M. Fukizawa[1], T. Sakanoi[1], Y.-M. Tanaka[2, 3, 4], Y. Ogawa[2, 3, 4], K. Hosokawa[5], Björn Gustavsson[6], Kirsti Kauristie[7], Alexander Kozlovsky[8], Tero Raita[8], Urban Brändström[9], Tima Sergienko[9]

[1] Graduate School of Science, Tohoku University, Sendai, Japan

[2] National Institute of Polar Research, Tachikawa, Japan

[3] Polar Environment Data Science Center, Joint Support-Center for Data Science Research, Research Organization of Information and Systems, Tokyo, Japan

[4] Department of Polar Science, The Graduate University for Advanced Studies, SOKENDAI, Japan

[5] Graduate School of Informatics and Engineering, University of Electro-Communications, Chofu, Japan

[6] Institute for Physics and Technology, Arctic University of Norway UiT, Tromsø, Norway

[7] Arctic Research Centre, Finnish Meteorological Institute, Helsinki, Finland

[8] Sodankylä Geophysical Observatory, University of Oulu, Oulu, Finland

[9] IRF-Swedish Institute of Space Physics, Kiruna, Sweden

Corresponding author: Mizuki Fukizawa (fukizawa.m@pparc.gp.tohoku.ac.jp)

Key Points:

- Computed tomography was applied to pulsating auroral patches for the first time.
- The electron flux and the three-dimensional volume emission rate were reconstructed using monochromatic auroral images from three stations.
- The ionospheric electron density was well reconstructed compared to that observed by European incoherent scatter radar.

Abstract

In recent years, auroral observation networks using high-sensitivity cameras have been developed in the polar regions. These networks allow us to observe dimmer auroras such as pulsating auroras (PsAs) with a high signal-to-noise ratio. We reconstructed the horizontal distribution of precipitating electrons using computed tomography with monochromatic PsA images obtained from three observation points. The three-dimensional distribution of the volume emission rate (VER) of the PsA was also reconstructed. The characteristic energy of the reconstructed precipitating electron flux ranged from 6 keV to 23 keV, and the peak altitude of the reconstructed VER ranged from 90 to 104 km. We evaluated the results using a model aurora and compared the model's electron density with the observed electron density. The electron density was reconstructed correctly to some extent. These results suggest that the horizontal distribution

of precipitating electrons associated with PsAs can be effectively reconstructed from ground-based optical observations.

**Plain Language Summary**

In recent years, auroral observation networks using high-sensitivity cameras have been developed in the polar regions. These networks allow us to observe dimmer auroras such as pulsating auroras (PsAs) with a high signal-to-noise ratio. Although precipitating electrons associated with pulsating auroras have been observed by rockets or satellites, PsA intensity periodicities of a few seconds make it difficult for such observations to distinguish between temporal and spatial changes. We can reconstruct the horizontal distribution of electrons causing auroral emission from auroral images obtained at multiple observation points using computed tomography. In this study, we applied computed tomography to PsAs for the first time and evaluated the reconstructed results using a model aurora and the observed electron density.

## 1 Introduction

Aurora computed tomography (ACT) is a method for reconstructing the three-dimensional (3-D) volume emission rate (VER) of auroral emission based on monochromatic auroral images obtained from multiple observation points (e.g., Aso et al., 1990). The horizontal distribution of precipitating electron flux can be simultaneously obtained by ACT without rocket or satellite observations (Tanaka et al., 2011). Previous studies have applied ACT to bright and well-shaped discrete auroras, such as the quiet arc during the substorm growth phase and multiple auroral arcs (Aso et al., 1990, 1993, 1998; Frey et al., 1996; Nygrén et al., 1997; Tanaka et al., 2011). However, ACT has not been applied to pulsating auroras (PsAs).

A PsA is a type of diffuse aurora that appears as irregular patches showing quasi-periodic on–off switching of its intensity with a periodicity of ~2–20 s (Yamamoto, 1988). The intensity is somewhat dimmer than that of a typical discrete aurora (some hundreds of R up to tens of kR at 557.7 nm; a few hundred R to ~10 kR at 427.8 nm) (McEwen et al., 1981). It has been difficult to apply ACT to PsAs because the signal-to-noise ratio (SNR) of PsA images is lower than those of discrete aurora images. However, remote operation of many high-sensitivity cameras via the internet and an archive system capable of storing a massive amount of aurora data make it possible to observe PsAs with a high SNR.

The Magnetometers–Ionospheric Radars–Allsky Cameras Large Experiment (MIRACLE) network consists of nine all-sky cameras (ASCs) located in the Fennoscandian region. Two of the ASCs with intensified charge-coupled devices (ICCDs) were replaced with cameras possessing the newer technology of electron-multiplying CCDs (EMCCDs) in 2007 (Sangalli et al., 2011). Ogawa et al. (2020) developed a low-cost multi-wavelength imaging system for aurora and airglow studies and installed Watec monochromatic imagers (WMIs) at several locations in the north and south polar regions. A WMI consists of

a highly sensitive CCD camera made by Watec Co., Ltd (Japan). These cameras are suitable for studying very faint auroral structures such as PsAs. In this study, we attempted to use these high-sensitivity cameras and ACT methods to reconstruct the 3-D VER of a PsA and the horizontal distribution of precipitating electrons for the first time.

## 2 Data and Methods

MIRACLE ASCs observed PsA patches from Kilpisjärvi (KIL, 69.05°N, 20.36°E), Abisko (ABK, 68.36°N, 18.82°E), and WMI ASCs at Skibotn (SKB, 69.35°N, 18.82°E) during the substorm recovery phase from 0:00 UT to 2:00 UT on 18 February 2018. These ASCs have a typical field-of-view, as shown in Figure 1b. The position of Tromsø (TRO, 69.58°N, 19.23°E) where the European incoherent scatter (EISCAT) radar operates is also shown. We selected 427.8-nm auroral images in which PsA patches were detected at the EISCAT radar observation point as observational data with which to compare reconstructed results. Figure 1a shows 427.8-nm auroral images obtained by the three ASCs from 00:53:30 UT to 00:53:42 UT. The temporal resolution of each ASCs was 2 s. A median filter of 3 × 3 pixels was applied to auroral images to improve the SNR. We also composited auroral images obtained from four WMI CCD cameras of the same type at SKB. The auroral image at SKB has a time ambiguity of ~1–2 s. We determined the time when the auroral image was obtained by aligning the temporal changes in the PsA patch as shown in auroral images from ABK, KIL, and SKB.

The ACT method used in this study is based on the method proposed by Tanaka et al. (2011). We adopted an oblique coordinate system with the origin (O) at coordinates of (69.4°N, 19.2°E). The X-axis was anti-parallel to the horizontal component of the geomagnetic field, the Y-axis was eastward, and the Z-axis was anti-parallel to the geomagnetic field and perpendicular to the X-axis (see Figure 2 in Tanaka et al. (2011)). The simulation region ranged from −75 to 75 km, from −100 to 100 km, and from 80 to 180 km for the X-, Y-, and Z-axes, respectively. We set the energy ($E$) range to extend from 300 eV to 100 eV. This region was divided linearly into $n_x \times n_y \times n_z$ voxels along the X-, Y-, and Z-axes and logarithmically into $n_E$ bins in the $E$ direction. We set the parameters ($n_x$, $n_y$, $n_z$, $n_E$) to (75, 100, 50, 50), corresponding to a spatial mesh size of 2 × 2 × 2 km. These parameters were selected so that each voxels has at least one line-of-sight crossing from the pixels in the auroral images.

The differential flux of precipitating electrons was reconstructed by maximizing the posterior probability $P(\mathbf{f}|\tilde{\mathbf{g}})$, where $\mathbf{f}$ is a vector of the differential flux of precipitating electrons and $\tilde{\mathbf{g}}$ is a vector of gray levels at pixels in the auroral images obtained with ASCs. According to Bayes' theorem, the posterior probability $P(\mathbf{f}|\tilde{\mathbf{g}})$ is given by (Tanaka et al., 2011)

$$P(\mathbf{f}|\tilde{\mathbf{g}}) \propto \exp\left[-\frac{1}{2}\left\{(\tilde{\mathbf{g}}-\mathbf{g}(\mathbf{f}))^T \Sigma^{-1} (\tilde{\mathbf{g}}-\mathbf{g}(\mathbf{f})) + \frac{\|\nabla^2 \mathbf{f}\|^2}{\sigma^2}\right\}\right], \quad (1)$$

where $\mathbf{g}(\mathbf{f})$ is a vector of grey levels obtained from model $\mathbf{f}$ by solving the forward problem (Eq. 8 in Tanaka et al. (2011)). $\Sigma^{-1}$ is the inverse covariance matrix, $\sigma$ is the variance of $\nabla^2\mathbf{f}$, and the second-order derivative of $\mathbf{f}$ is taken with respect to $x$, $y$, and $E$. We determined $\Sigma^{-1}$ from the standard deviation calculated from the $32 \times 32$-pixel region in each auroral image. The region

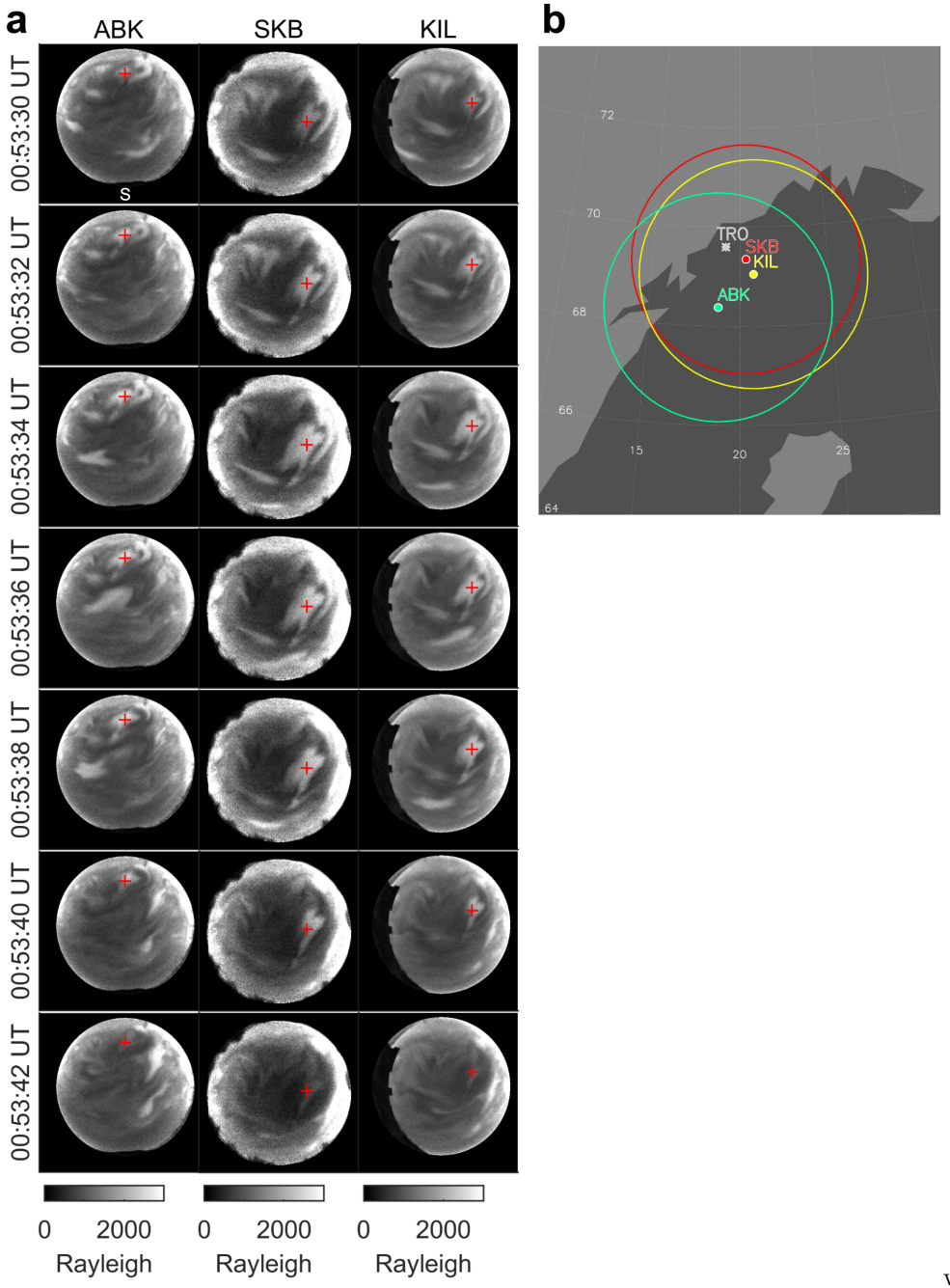


was determined to contain a relatively flat region. To maximize the posterior probability, it is necessary to minimize the function

$$\varphi\left(\mathbf{f};\ w,\ \lambda,\ \lambda_E,\ c_j\right) = \sum_j \left(c_j\tilde{\mathbf{g}}_j - \mathbf{g}_j\left(\mathbf{f}\right)\right)^T \Sigma^{-1}\left(c_j\tilde{\mathbf{g}}_j - \mathbf{g}_j\left(\mathbf{f}\right)\right) + \lambda^2\left\|\nabla^2_{x,\ y}\mathbf{f} + \lambda_E^2\nabla_E^2\mathbf{f}\right\|^2, \quad (2)$$

where $j$ signifies the three observation points (ABK, KIL, and SKB). $\lambda$, $\lambda_E$, and $c_j$ are the so-called hyperparameters, which are constants corresponding to the weighting factors for the spatial ($\lambda$) and energy ($\lambda_E$) normalization terms and the correction factors for the relative sensitivity between cameras ($c_j$).

We carried out the change of variables $\mathbf{f} = \exp\left(\mathbf{x}\right)$ to take advantage of the non-negative constraint on the differential flux $\mathbf{f}$ (i.e., $\mathbf{f} \geq 0$). We then minimized the function $\varphi\left(\mathbf{x};\ \lambda,\ \lambda_E,\ c_j\right)$ by implementing the Gauss–Newton algorithm with the initial value $\mathbf{x}^{(0)} = \log\left(\mathbf{f}^{(0)}\right)$, where $\mathbf{f}^{(0)} = 10^7$ [m$^{-2}$ s$^{-1}$ eV$^{-1}$]. The iteration number was set to be 200.

The hyperparameters were determined using the fivefold cross-validation method (Stone, 1974). Sect. 3.3 of Tanaka et al. (2011) explains the details.

The PsA patches shown in Figure 1a are embedded in the background diffuse auroral emission. We found that a horizontally uniform diffuse aurora causes ambiguity in the reconstruction result because the altitude of the uniform auroral structure cannot be determined from the single-wavelength images. Thus, we subtracted the background emission from the images prior to ACT reconstruction. We created the background emission image by assuming the same value for all voxels. The background VER was taken to be 75 cm$^{-3}$ s$^{-1}$, corresponding to the spatially averaged observed background emission intensity.

## 3 Results and Discussion

### 3.1 Reconstruction of a model pulsating aurora patch

We reconstructed a model PsA patch from pseudo auroral images to evaluate the analytical error of ACT before reconstructing the PsA patch from the observed auroral images. To create the pseudo auroral images, we prepared the horizontal distributions of the total energy, $Q_0$, and the characteristic energy, $E_c$. We then derived the 3-D VER, $L$, as shown in Figure 2a. The total energy was assumed to have a Gaussian shape in horizontal directions with a maximum value of 6 mW m$^{-2}$. The energy distribution was considered to be a Maxwellian distribution with an isotropic characteristic energy of 15 keV. Pseudo auroral images were obtained from $L$ by solving the forward problem (Figure 2b). We added random noise from a normal distribution with a mean value of 0 and the standard deviation determined from observed auroral images.

Figure 2c shows $Q_0$, $E_c$, and $L$ reconstructed from the pseudo auroral images. The values of $Q_0$ were calculated as $Q_0 = \sum_i E_i f\left(E_i\right)\left(E_{i+1} - E_i\right)$. When we assume the energy distribution to be a Maxwellian distribution, the characteristic energy can be written as $E_c = \frac{1}{2}\left\langle E\right\rangle = \frac{1}{2}\frac{Q_0}{\sum_i f(E_i)(E_{i+1}-E_i).}$. We calculated the errors between the model and the result for $Q_0$, $E_c$, and $L$ (Figure 2d). The median values of the errors were $-5\%$ for $Q_0$, $-21\%$ for $E_c$, and $-11\%$ for $L$. The

northwestern part of $Q_0$ was overestimated by at most 23%, the edge part was underestimated by at most 29%, and the central part was underestimated by ~8%. The central part of $E_c$ was reconstructed with similar accuracy. In comparison, the edge part (especially the northwestern part) was underestimated by at most 56%. The underestimation of $E_c$ was caused by the overestimation of the emission altitude (Figure 2d). Information regarding the PsA emission altitude is easily lost in obtaining the auroral image, since the structure of the PsA patch is vertically thin and horizontally wide. In addition, the SNR at the edge part is lower than at the central part, since we assumed a Gaussian shape for the horizontal distribution of $Q_0$. These factors would tend to reduce the accuracy at the edge part.

It should be noted that the reconstructed results using the hyperparameters determined by the cross-validation method revealed unexpected fine structures. To avoid this phenomenon, we set the lower limit of $\lambda$ by a different method, namely by minimizing the residual sum of squares

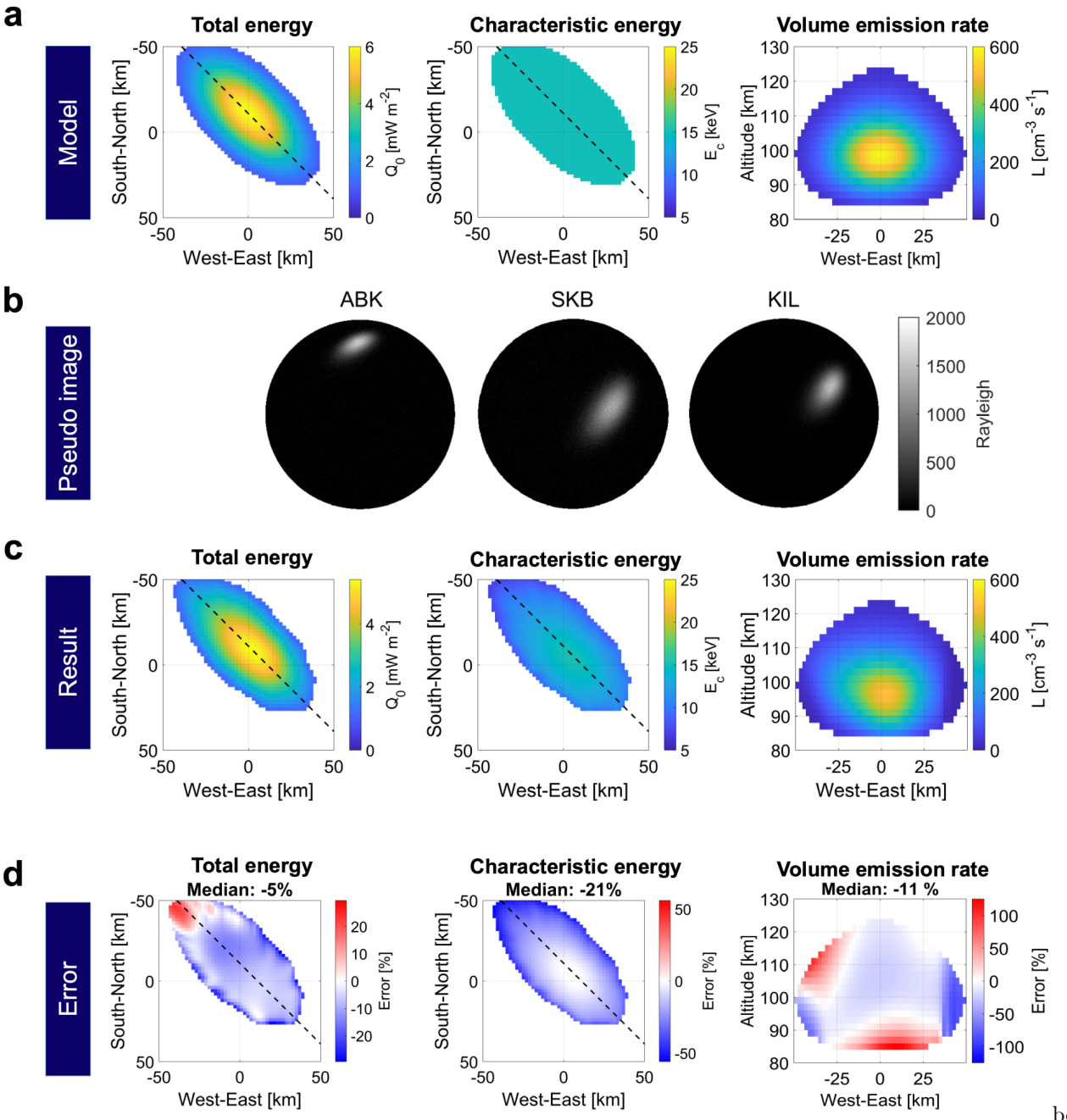


be

the model and the reconstructed result of $Q_0$ and $E_c$. The lower limit on $\lambda$ makes it challenging to reconstruct actual fine-scale structures in the patches.

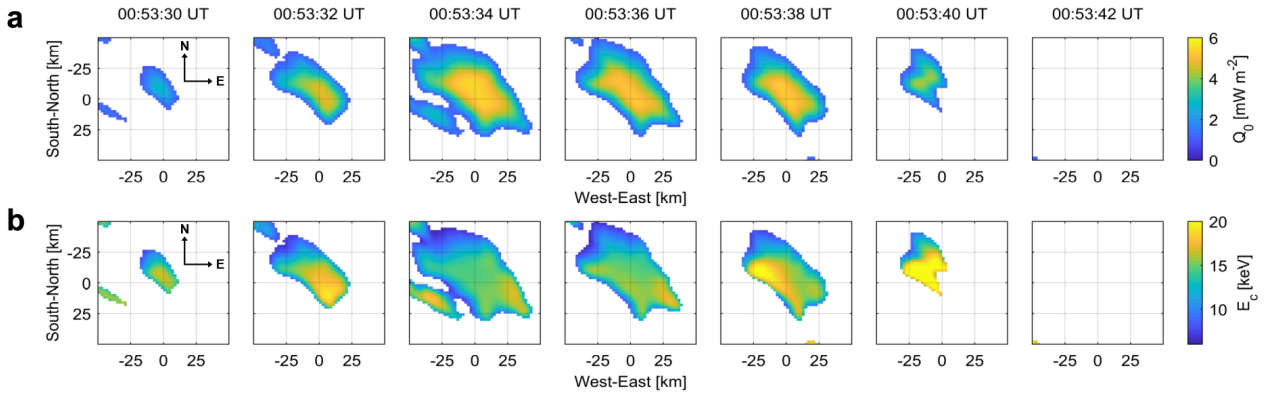


3.2 Precipitating electrons

Figures 3a and 3b show $Q_0$ and $E_c$ as reconstructed from the observed auroral images (Figure 1a). The maximum value of $Q_0$ was ~6 mW m$^{-2}$. The reconstructed $E_c$ ranged from 6 keV to 23 keV. These energies are consistent with observation results from sounding rockets and low-altitude satellites (e.g., McEwen et al., 1981; Miyoshi et al., 2015). We found that the horizontal distribution of $E_c$ was neither uniform nor stable in the patch during the pulsation. In particular, the southwestern part of $E_c$ was enhanced at 00:53:38 UT. It should be noted that the edge and northwestern parts of $E_c$ are expected to be underestimated due to analytical error, as shown in Figure 2d. These temporal variations indicate changes in the cyclotron resonance energy of whistler-mode chorus waves during the pulsation. The chorus waves scatter electrons into a loss cone near the magnetic equator. The cyclotron resonance energy of chorus waves depends on the background magnetic field, electron density, and wave frequency (e.g., Kennel & Petschek, 1966). The observed temporal variations thus indicate changes in the magnetospheric source region's background magnetic or plasma environment during the pulsation. Thus, the ACT method is helpful for investigating PsA-associated temporal variations in the horizontal distribution of precipitating electrons without rocket or satellite observations.

3.3 Volume emission rate

Figure 4a shows the 3-D distributions of VERs derived from the reconstructed electron flux by solving the forward problem. Cross-sections in the horizontal plane at an altitude of 94 km are shown in Figure 4b. The peak altitude ranges from 90 to 104 km (Figure 4c). The error of the peak altitude is shown in Figure 4d. The high peak altitude at the northwestern part is expected to be overestimated by at most 8% due to analytical error, as shown in Figure 2d. The full width at half maximum is almost isotropic with a median value of ~20 km (Figure 4e). For the most part, the altitude width is expected to be overestimated by ~2% (Figure 4f). The reconstructed peak altitude and width are consistent with those determined in previous studies using stereoscopic observations or an incoherent scatter radar (Brown et al., 1976; S. L. Jones et

al., 2009; Kataoka et al., 2016). (Stenbaek-Nielsen & Hallinan, 1979) reported the existence of thin (<1 km vertical extent) PsA patches based on stereoscopic observations, but our results do not support their results.

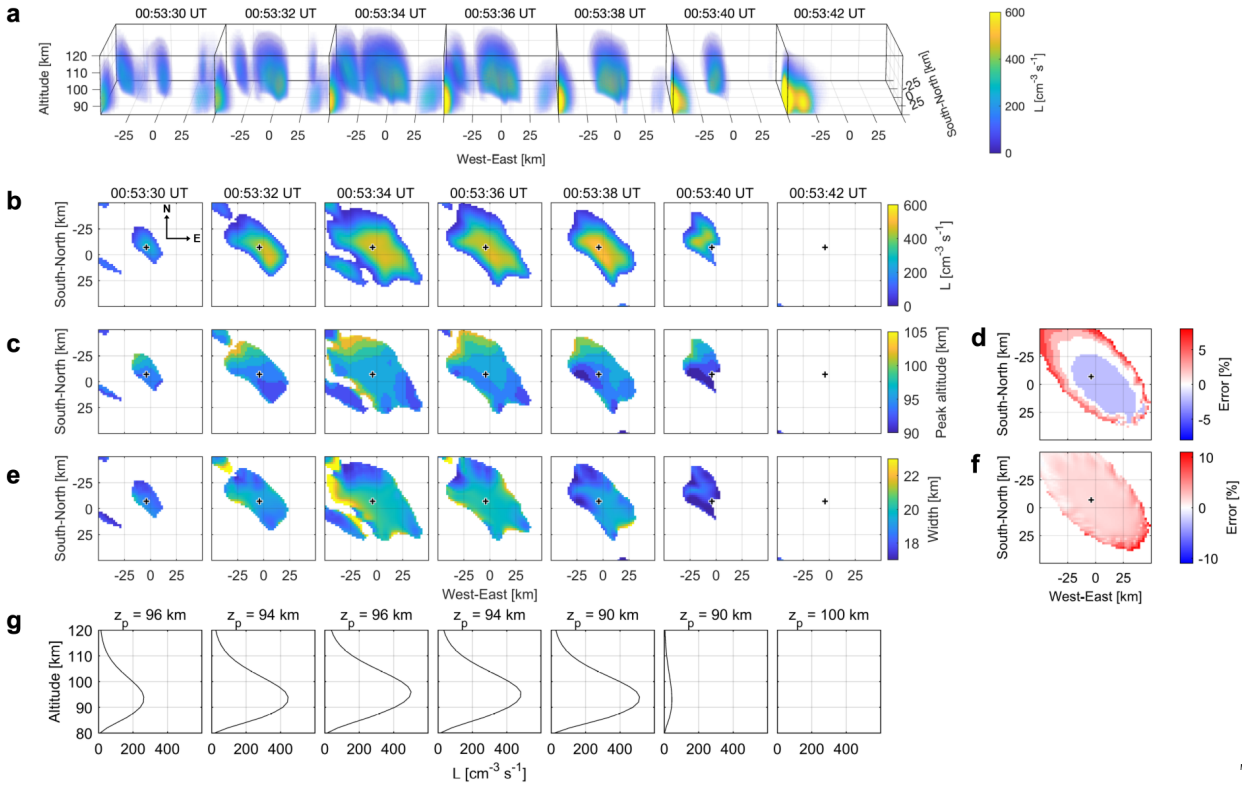


peak altitude of the PsA patch was also estimated by a different. We projected the observed auroral images at altitudes ranging from 80 km to 120 km with an interval of 2 km (Movie S1). The emission altitude was determined to be the altitude at which the residual squared sum between the two projected images reached a minimum value (Figure S1). The estimated peak altitude range was 92 to 106 km from 00:53:30 UT to 00:53:40 UT (Figure S2). These altitudes closely match those determined by ACT.

### 3.4 Electron density

The altitude profiles of VER at the EISCAT radar observation point shown in Figure 4g were converted to an ionospheric electron density and compared with the actual data observed by the EISCAT radar. The continuity equation for the electron density can be written as

$$\frac{\partial n_e}{\partial t} = kL - \alpha_{\mathrm{eff}} n_e^2, \quad (3)$$

where $n_e$ [$m^{-3}$] is the electron density, $L$ [$m^{-3}$ $s^{-1}$] is the VER, $k$ is a positive constant for converting VER to the ionization rate (see Appendix), and $\alpha_{\mathrm{eff}}$ [$m^3$ $s^{-1}$] is the effective recombination rate. We derived the electron density from the VER by solving Eq. 3 with the Runge–Kutta method. The initial value was derived from Eq. 3 under steady-state conditions (i.e., $\partial n_e/\partial t = 0$) using reconstructed $L$ at 00:53:36 UT. The VERs were interpolated linearly in order to use the Runge–Kutta method. The altitude profile of $\alpha_{\mathrm{eff}}$ has been investigated by several studies using rocket- and ground-based measurements. Vickrey et al. (1982) summarized many of these results and proposed the following best fit parameterization:

$$\alpha_{\mathrm{fit}} = 2.5 \times 10^{-12} \exp\left(-z/51.2\right) \ \left[m^3\ s^{-1}\right], \quad (4)$$

where $z$ [km] is the altitude. Semeter & Kamalabadi (2005) used the effective recombination coefficients $\alpha_{\mathrm{NO}^+}$ and $\alpha_{O_2^+}$ for $NO^+$ and $O_2{}^+$, respectively (Walls & Dunn, 1974), as upper and lower bounds on $\alpha_{\mathrm{eff}}$:

$$\alpha_{\mathrm{NO}^+} = 4.2 \times 10^{-13} \left(300/T_n\right)^{0.85} \ \left[m^3\ s^{-1}\right], \quad (5)$$

$$\alpha_{O_2^+} = 1.95 \times 10^{-13} \left(300/T_n\right)^{0.7} \ \left[m^3\ s^{-1}\right]. \quad (6)$$

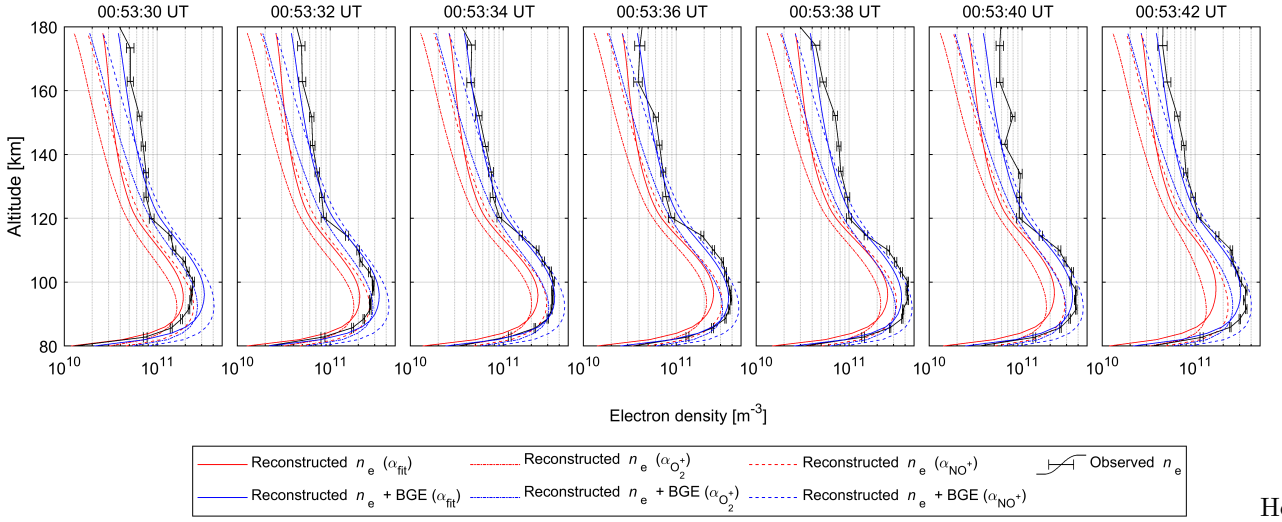


H

$T_{\mathrm{n}}$ [K] is the neutral temperature. The red lines in Figure 5 show the derived electron densities using these three recombination coefficients. We note that these values are underestimated compared to the electron densities observed by the EISCAT radar (black lines in Figure 5). This underestimation probably comes from the background emission subtraction from the auroral images prior to ACT and from ambiguity in the effective recombination coefficients.

The electron densities reconstructed from auroral images without background emission subtraction are shown as blue lines for reference in Figure 5. The reconstruction results from the images, including background emission, approached the electron density profile observed with the EISCAT radar. We noted that the electron density was reconstructed correctly to some extent after the auroral emission intensity decreased at 00:53:40 UT. This correct reconstruction is due to incorporation of the time derivative term in the continuity equation. The electron density would seem to have rapidly decreased after 00:53:40 UT if the time derivative term were not considered. This result suggests that the time derivative term should be considered when using the continuity equation (Eq. (3)) to derive electron densities associated with PsAs.

It should be noted that the electron density is still underestimated at higher altitudes (>~140 km) even if the background emission was included. This underestimation would be improved by reconstructing low-energy electron flux from auroral images of various wavelengths (e.g., 844.6 nm).

## 4 Conclusions

We applied the ACT method to PsA patches for the first time and reconstructed the horizontal distribution of precipitating electrons from 427.8-nm auroral images obtained from three observation points. We improved the previously proposed ACT method by adding the following processes: the subtraction of the background diffuse aurora from the auroral images prior to ACT, the estimation of the relative sensitivity between ASCs, and the determination of the hyperparameters of the regularization term. The characteristic energies of the reconstructed electron fluxes (6 keV to 23 keV) and the peak altitudes of the reconstructed VERs (90 to 104 km) were consistent with those found in previous studies. We determined that the horizontal distribution of the characteristic energy was neither uniform nor stable in the patch during the pulsation, further underlining the shortcomings of rocket and satellite observations for investigating PsAs. ACT error was evaluated using a model auroral patch. The characteristic energy of electron flux was correctly reconstructed at the center part of the patch but underestimated at the patch edge by at most 56%. The reconstructed electron flux will be improved in future work by incorporating auroral images of various wavelengths.

Although we reconstructed the differential flux of precipitating electrons from auroral images using ACT, Tanaka et al. (2011) extended ACT to a method called generalized-ACT (G-ACT). G-ACT uses multi-instrument data, such as ionospheric electron density from incoherent scatter radar, cosmic noise absorption from imaging riometers, and the auroral images. They demonstrated that the incorporation of the ionospheric electron density from the EISCAT radar improved the accuracy of the reconstructed electron flux. Furthermore, 3-D ionospheric observation by EISCAT_3D (http://www.eiscat3d.se) is scheduled to begin in 2023. In the future, we will improve the reconstructed electron flux by conducting G-ACT using electron density data from the EISCAT or EISCAT_3D radar.

Appendix

**Derivation of $k$**

In this section, we describe how to obtain the positive constant $k(z)$ in Sect. 3.4. The $N_2^+$ (427.8 nm) emission is due to the transition from $N_2^+$ $\left(B^2\Sigma_u^+\right)_{v=0}$ to $N_2^+$ $\left(X^2\Sigma_g^+\right)_{v=1}$. According to Sergienko & Ivanov (1993), the VER $L(z)$ [$\mathrm{m^{-3}\ s^{-1}}$] is approximated by

$$L(z) = \frac{A_{0-1}q_{0-0}}{\sum_v A_{0-v}} w(z) = \frac{A_{0-1}q_{0-0}}{\sum_v A_{0-v}} \frac{p(z)\varepsilon(z)}{\Delta\varepsilon}, \quad \text{(A1)}$$

where $A_{0-1}$ is the Einstein coefficient for the transition from $N_2^+$ $\left(B^2\Sigma_u^+\right)_{v=0}$ to $N_2^+$ $\left(X^2\Sigma_g^+\right)_{v=1}$, $w(z)$ [$\mathrm{m^{-3}\ s^{-1}}$] is the production rate of $N_2^+$ $\left(B^2\Sigma_u^+\right)$, $q_{0-0}$ is the Franck–Condon factor for the electronic transition from $N_2^+$ $\left(X^1\Sigma_g^+\right)_{v=0}$ to $N_2^+$ $\left(B^2\Sigma_u^+\right)_{v=0}$, $p(z)$ is the probability that $\varepsilon(z)$ excites $N_2$, $\varepsilon(z)$ [$\mathrm{eV\ m^{-3}\ s^{-1}}$] is the energy deposition rate, and $\Delta\varepsilon$ [eV] is the excitation energy cost of $N_2^+$ $\left(B^2\Sigma_u^+\right)$. The ionization rate due to the precipitating electrons $q_{\mathrm{ion}}(z)$ [$\mathrm{m^{-3}\ s^{-1}}$] is given by

$$q_{\mathrm{ion}}(z) = \frac{\varepsilon(z)}{\Delta\varepsilon_{\mathrm{ion}}}, \quad \text{(A2)}$$

where $\Delta\varepsilon_{\mathrm{ion}}$ [eV] is the energy used to produce an ion–electron pair. Substituting Eq. (A1) into Eq. (A2) gives

$$q_{\mathrm{ion}}(z) = \frac{\sum_v A_{0-v}}{A_{0-1}q_{0-0}} \frac{\Delta\varepsilon}{\Delta\varepsilon_{\mathrm{ion}}} \frac{1}{p(z)} L(z). \quad \text{(A3)}$$

Therefore, the positive constant $k(z)$ for converting VER to the ionization rate is

$$k(z) = \frac{\sum_v A_{0-v}}{A_{0-1}q_{0-0}} \frac{\Delta\varepsilon}{\Delta\varepsilon_{\mathrm{ion}}} \frac{1}{p(z)}. \quad \text{(A4)}$$

The parameters used for the calculation are summarized in Table S1.

Acknowledgments

The first author is a Research Fellow of the Japan Society for the Promotion of Science (DC). This study is supported by JSPS Bilateral Open Partnership Joint Research Projects, JSPS KAKENHI Grant Numbers JP17K05672, JP20J11829, and JP21H01152. We thank Kirsti Kauristie, Kellinsalmi Mir-

jam, and Carl-Fredrik Enell for maintaining the MIRACLE camera network and data flow. EISCAT is an international association supported by research organizations in China (CRIRP), Finland (SA), Japan (NIPR), Norway (NFR), Sweden (VR), and the United Kingdom (UKRI). The database construction for the imager data at Skibotn and the EISCAT radar data has been supported by the IUGONET (Inter-university Upper atmosphere Global Observation NETwork) project (http://www.iugonet.org/). The EISCAT data are available at http://pc115.seg20.nipr.ac.jp/www/AQVN/evs1.html. The imager data at Skibotn can be obtained at http://pc115.seg20.nipr.ac.jp/www/AQVN/evs1.html.

References

Aso, T., Hashimoto, T., Abe, M., Ono, T., & Ejiri, M. (1990). On the analysis of aurora stereo observations. *Journal of Geomagnetism and Geoelectricity*, *42*(5), 579–595. https://doi.org/10.5636/jgg.42.579Aso, T., Ejiri, M., Miyaoka, H., Hashimoto, T., Abu, T. Y., & Abe, M. (1993). Aurora stereo observation in Iceland. *Proceedings of the NIPR Symposium on Upper Atmosphere Physics*, *6*, 1–14.Aso, T., Ejiri, M., Urashima, A., Miyaoka, H., Steen, Å., Brändstrom, U., & Gustavsson, B. (1998). First results of auroral tomography from ALIS-Japan multi-station observations in March, 1995. *Earth, Planets and Space*, *50*(1), 81–86. https://doi.org/10.1186/BF03352088Brown, N. B., Davis, T. N., Hallinan, T. J., & Stenbaek-Nielsen, H. C. (1976). Altitude of pulsating aurora determined by a new instrumental thechnique. *Geophysical Research Letters*, *3*(7), 403–404. https://doi.org/10.1029/GL003i007p00403Frey, S., Frey, H. U., Carr, D. J., Bauer, O. H., & Haerendel, G. (1996). Auroral emission profiles extracted from three-dimensionally reconstructed arcs. *Journal of Geophysical Research: Space Physics*, *101*(A10), 21731–21741. https://doi.org/10.1029/96ja01899Jones, A. V. (1974). *Aurora*. Dordrecht: D. Reidel Publishing Company. https://doi.org/10.1007/978-94-010-2099-2Jones, S. L., Lessard, M. R., Fernandes, P. A., Lummerzheim, D., Semeter, J. L., Heinselman, C. J., et al. (2009). PFISR and ROPA observations of pulsating aurora. *Journal of Atmospheric and Solar-Terrestrial Physics*, *71*(6–7), 708–716. https://doi.org/10.1016/j.jastp.2008.10.004Kataoka, R., Fukuda, Y., Uchida, H. A., Yamada, H., Miyoshi, Y., Ebihara, Y., et al. (2016). High-speed stereoscopy of aurora. *Annales Geophysicae*, *34*(1), 41–44. https://doi.org/10.5194/angeo-34-41-2016Kennel, C. F., & Petschek, H. E. (1966). Limit on stably trapped particle fluxes. *Journal of Geophysical Research*, *71*(1), 1–28. https://doi.org/10.1029/JZ071i001p00001McEwen, D. J., Yee, E., Whalen, B. A., & Yau, A. W. (1981). Electron energy measurements in pulsating auroras. *Canadian Journal of Physics*, *59*(8), 1106–1115. https://doi.org/10.1139/p81-146Miyoshi, Y., Saito, S., Seki, K., Nishiyama, T., Kataoka, R., Asamura, K., et al. (2015). Relation between energy spectra of pulsating aurora electrons and frequency spectra of whistler-mode chorus waves. *Journal of Geophysical Research: Space Physics*, *120*(9), 7728–7736. https://doi.org/10.1002/2015JA021562.Nygrén, T., Markkanen, M., Lehtinen, M., & Kaila, K. (1997). Application of stochastic inversion in auroral tomography. *Annales Geophysicae*, *14*(11), 1124–1133.

https://doi.org/10.1007/s00585-996-1124-1Ogawa, Y., Tanaka, Y., Kadokura, A., Hosokawa, K., Ebihara, Y., Motoba, T., et al. (2020). Development of low-cost multi-wavelength imager system for studies of aurora and airglow. *Polar Science*, *23*(April 2019). https://doi.org/10.1016/j.polar.2019.100501Picone, J. M., Hedin, A. E., Drob, D. P., & Aikin, A. C. (2002). NRLMSISE-00 empirical model of the atmosphere: Statistical comparisons and scientific issues. *Journal of Geophysical Research: Space Physics*, *107*(A12), SIA 15-1-SIA 15-16. https://doi.org/10.1029/2002JA009430Sangalli, L., Partamies, N., Syrjäsuo, M., Enell, C. F., Kauristie, K., & Mäkinen, S. (2011). Performance study of the new EMCCD-based all-sky cameras for auroral imaging. *International Journal of Remote Sensing*, *32*(11), 2987–3003. https://doi.org/10.1080/01431161.2010.541505Semeter, J., & Kamalabadi, F. (2005). Determination of primary electron spectra from incoherent scatter radar measurements of the auroral e region. *Radio Science*, *40*(2), n/a-n/a. https://doi.org/10.1029/2004RS003042Sergienko, T., & Ivanov, V. (1993). A new approach to calculate the excitation of atmospheric gases by auroral electron impact. *Annales Geophysicae- European Geophysical Society*, *11*(8), 717–727.Stenbaek-Nielsen, H. C., & Hallinan, T. J. (1979). Pulsating auroras: Evidence for noncollisional thermalization of precipitating electrons. *Journal of Geophysical Research*, *84*(A7), 3257–3271. https://doi.org/10.1029/JA084iA07p03257Stone, M. (1974). Cross-validatory choice and assessment of statistical predictions (with discussion). *Journal of the Royal Statistical Society: Series B (Methodological)*, *38*(1), 102–102. https://doi.org/10.1111/j.2517-6161.1976.tb01573.xTanaka, Y. M., Aso, T., Gustavsson, B., Tanabe, K., Ogawa, Y., Kadokura, A., et al. (2011). Feasibility study on Generalized-Aurora Computed Tomography. *Annales Geophysicae*, *29*(3), 551–562. https://doi.org/10.5194/angeo-29-551-2011Vickrey, J. F., Vondrak, R. R., & Matthews, S. J. (1982). Energy deposition by precipitating particles and Joule dissipation in the auroral ionosphere. *Journal of Geophysical Research: Space Physics*, *87*(A7), 5184–5196. https://doi.org/10.1029/ja087ia07p05184Walls, F. L., & Dunn, G. H. (1974). Measurement of total cross sections for electron recombination with NO + and O 2 + using ion storage techniques. *Journal of Geophysical Research*, *79*(13), 1911–1915. https://doi.org/10.1029/ja079i013p01911Yamamoto, T. (1988). On the temporal fluctuations of pulsating auroral luminosity. *Journal of Geophysical Research*, *93*(A2), 897–911. https://doi.org/10.1029/JA093iA02p00897